

Signal Simulator for Starlink Ku-Band Downlink

Zacharias M. Komodromos[†], Wenkai Qin^{*}, Todd E. Humphreys^{*}

^{*}*Department of Aerospace Engineering and Engineering Mechanics, The University of Texas at Austin*

[†]*Department of Electrical and Computer Engineering, The University of Texas at Austin*

ABSTRACT

This paper summarizes the current-known model for Starlink’s Ku-band downlink signal and develops a platform for simulating a received signal. The simulator models key elements of the signal structure, along with channel effects such as noise, delay, and Doppler. Further, this paper outlines a hypothesis testing detection process for acquisition of a Starlink downlink frame. The information in this paper will be of general interest to those seeking to understand the Starlink waveform, but is particularly targeted to those wishing to exploit Starlink as an alternative to GNSS for position, navigation, and timing (PNT). The simulator can also make use of precise ephemerides to generate more faithful signals. Theoretical limits on the minimum signal-to-noise ratio required to detect a frame are presented and supported by simulated signals. Finally, the hypothesis testing detection process is applied to live-captured Starlink data.

I. BIOGRAPHIES

Zacharias M. Komodromos (B.S., Iowa State University) is a Ph.D. student in the Department of Electrical and Computer Engineering at The University of Texas at Austin and a member of the UT Radionavigation Laboratory. His research interests include wireless communications and re-purposing broadband Internet satellites for positioning, navigation, and timing.

Wenkai Qin (B.S., Harvey Mudd College) is a Ph.D. student in the Department of Aerospace Engineering and Engineering Mechanics at The University of Texas at Austin and a graduate research assistant in the UT Radionavigation Laboratory. His current research interests include LEO PNT, swarm-based navigation, and SLAM.

Todd E. Humphreys (B.S., M.S., Utah State University; Ph.D., Cornell University) holds the Ashley H. Priddy Centennial Professorship in Engineering in the Department of Aerospace Engineering and Engineering Mechanics at the University of Texas at Austin. He is Director of the Wireless Networking and Communications Group and of the UT Radionavigation Laboratory, where he specializes in the application of optimal detection and estimation techniques to positioning, navigation, and timing. His awards include the UT Regents’ Outstanding Teaching Award (2012), the NSF CAREER Award (2015), the ION Thurlow Award (2015), the PECASE (NSF, 2019), and the ION Kepler Award (2023). He is Fellow of the Institute of Navigation and of the Royal Institute of Navigation.

II. INTRODUCTION

Low Earth orbit satellite (LEO) constellations designed for broadband communication have been the subject of recent studies in positioning, navigation, and timing (PNT). Among the various LEO constellations, Starlink’s constellation has been the most popular mainly due to its higher number of deployed satellite vehicles (SV) and thus coverage, with plans for up to 42,000 SVs in LEO [SpaceX, 2021] according to filings to the U.S. Federal Communications Commission.

With regards to PNT, some literature has explored the benefits of dual-purposing communications constellations for PNT in a cooperative or fused fashion, showing how using just 1.6% of the downlink capacity could provide pseudorange superior to traditional GNSS [Iannucci and Humphreys, 2020], [Iannucci and Humphreys, 2022]. Other literature has specifically explored using Starlink’s constellation for opportunistic PNT, where Doppler-based and carrier-phase-based positioning has been demonstrated to work with Starlink using a 2.5-MHz-wide receiver [Neinavaie et al., 2021], [Neinavaie et al., 2022], [Khalife et al., 2022], and a 1-MHz-wide receiver [Jardak and Adam, 2023].

A more advantageous method would be to make use of the underlying communications signal transmitted by Starlink. More recent work in [Humphreys et al., 2023] has revealed details about the Starlink signal structure that could enable pseudorange-based positioning, providing timing better than doppler-based positioning in the range of 100 μ s [Psiaki, 2021]. Given that a single Starlink channel spans 240MHz, the receiver one must maintain in order to opportunistically capture entire Starlink channels is cumbersome. A tool that generates realistic Starlink signals would enable many without the necessary equipment to study the signals. This is especially the case for pseudorange PNT-based inquiries since at least four SV signals are required for instantaneous multi-laterated position and time determination without *a priori* constraints [Reid et al., 2020].

Signal toolboxes for simulating, analyzing, and configuring popular communication signal standards (e.g. LTE) have long been useful, so the goal of this paper is to provide a similar simulator to address the rising popularity of Starlink. The simulator, named the University of Texas Starlink Signal Simulator, is based on the signal structure and findings published in [Humphreys et al., 2023] and aims to support study of the signals both for communications and PNT.

While our simulator could opt for a stochastic geometry approach to generating realistic parameters, such as in [Okati and Riihonen, 2022], we favor a different approach. The simulator intakes ephemeris information for Starlink SVs, provided publicly by SpaceX [Sta, 2023] or through NORAD, in order to generate more faithful simulations compared to stochastic-dependent generations. By providing the simulator with ephemerides treated as the truth, the simulated signals can be used to study the communication signal for PNT purposes. Additionally, with the true ephemerides and a user-desired location for the receiver, modeling Doppler and pathloss effects is trivial.

To validate a signal's presence, this paper showcases a Neyman-Pearson hypothesis testing approach. There are many such analyses for non-data-aided scenarios, those agnostic to the data carried by the symbols, such as [Xu, 2014] which makes use of the cyclic prefix in OFDM symbols. Much work also exists in data-aided scenarios via matched filtering, such as [Du et al., 2021] and more generally [Borio et al., 2008]. Since symbols of the signal have already been revealed and are known to be common across all SVs, this paper adopts a data-aided approach, although if the signals change in the future, while still remaining as OFDM, the non-data aided approach could be used, or the process in [Humphreys et al., 2023] can be repeated to extract the new synchronization sequences. Leveraging hypothesis testing for signal detection, a complex ambiguity function (CAF) is formed and used for acquisition. Using acquisition methods described in this paper, one could further study the time of arrival of frames from Starlink SVs and characterize their timing stability.

While there is still much unknown about the scheduling of servicing satellite vehicles (SVs), beamforming details, and synchronization sequence cadence within the signal, enough is known such that a simulator can be formed in which some parameters can remain variable to accommodate for future adaptation. For example, the number of SVs serving a cell, or the number of cells that a single SV serves at a time is unconfirmed, and can be parametrized as a probability of observing a signal in a given channel. Further, it remains speculative just how many of the channels a Starlink SV uses, or how frequently it hops between them. While work in [Neinavaie and Kassas, 2022] and more recently in [Blázquez-García et al., 2023], provide the scale in which one can expect switching between satellites, this paper will depend on a provided binomial probability for observing the signal in its generation, and will be limited to a single channel due to the large file sizes a larger bandwidth generation would require.

This paper offers three contributions. First, Starlink downlink frame generation is presented, including all aforementioned signal effects. Second, statistics for signal detection and acquisition are developed, analyzed, and showcased. Third, the simulator will be used to generate a received signal to be processed for communications through extracting the data, and PNT through obtaining a time of arrival (TOA).

Notation: Column vectors are denoted with lowercase bold, e.g., \mathbf{x} . Scalars are denoted without bold, e.g., x . The n th entry of a vector \mathbf{x} is denoted $x(n)$. A sub-vector of a vector \mathbf{x} from the n th entry to the $(n + N)$ th entry is denoted $\mathbf{x}(n : n + N)$. The element-wise product, or Hadamard product, of two vectors \mathbf{x} and \mathbf{y} is denoted with $\mathbf{x} \odot \mathbf{y}$. Multidimensional vectors are also denoted with bold, e.g., \mathbf{X} . For a matrix with 3 dimensions, the m th i th k th entry is $X_{mi}(k)$, the m th i th vector is \mathbf{X}_{mi} , and the m th matrix is \mathbf{X}_m . Zero-based indexing is used throughout the paper.

III. SIGNAL STRUCTURE, PROPERTIES, AND MODEL

This paper adopts the nomenclature, signal models, and Starlink-specific parameters from [Humphreys et al., 2023]. A summary of the essential signal structure is presented in the following subsection, followed by models for Doppler and fading. Finally, our method for signal generation is introduced.

A. Signal Frame structure

A single Starlink frame consists of $N_{sf} = 302$ non-zero symbols, each $T_{sym} = 4.4 \mu s$ in duration followed by a frame guard interval $T_{fg} = 4.533 \mu s$ long, totaling a frame period $T_f = 1/750$ s. The first symbol is occupied by the primary synchronization sequence (PSS), which has a native time-domain representation. All other nonzero symbols are standard OFDM symbols. The first such symbol, occupying the second symbol interval, is the secondary synchronization sequence (SSS).

The OFDM symbols in each frame may be further described by their OFDM parameters, such as the cyclically-prepended guard interval duration $T_g = 0.133 \mu s$, number of subcarriers $N = 1024$, channel bandwidth $F_s = 240$ MHz, and subcarrier spacing $F = F_s/N$. For a pictorial view of the frame, refer to Fig. 1.

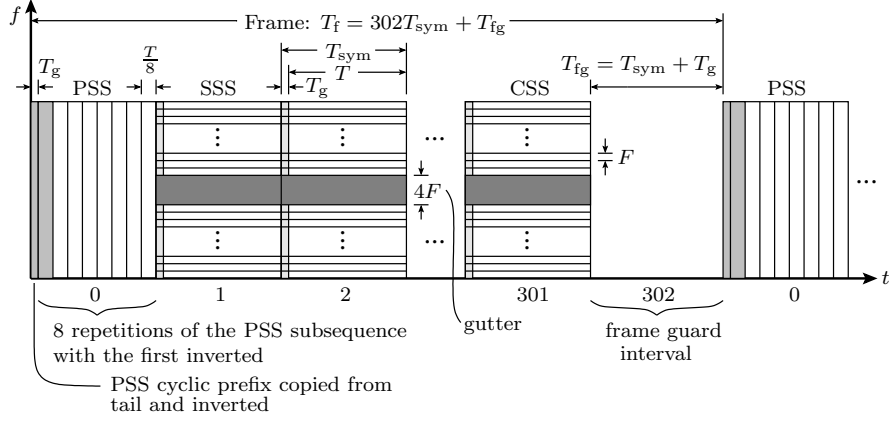


Fig. 1: Frame diagram from [Humphreys et al., 2023].

TABLE I: Starlink Downlink Signal Parameters from [Humphreys et al., 2023]

Name	Parameter	Value	Units
Channel bandwidth	F_s	240	MHz
Number of subcarriers in F_s	N	1024	
Number of cyclic prefix intervals	N_g	32	
Frame period	T_f	1/750	s
Frame guard interval	T_{fg}	$68/15 = 4.5\overline{33}$	μs
Number of non-zero symbols per frame	N_{sf}	302	
Number of data symbols in a frame	N_{sfd}	298	
Useful OFDM symbol interval	$T = N/F_s$	$64/15 = 4.2\overline{66}$	μs
Symbol guard interval	$T_g = N_g/F_s$	$2/15 = 0.1\overline{33}$	μs
OFDM symbol duration	$T_{sym} = T + T_g$	4.4	μs
Subcarrier spacing	$F = F_s/N$	234375	Hz
Center frequency of i th channel	F_{ci}	$10.7 + F/2 + 0.25(i - 1/2)$	GHz
Channel spacing	F_δ	250	MHz
Width of guard band between channels	F_g	10	MHz

The i th symbol of the m th frame is expressed as

$$x_{mi}(t) = \frac{1}{\sqrt{N}} \sum_{k=0}^{N-1} X_{mi}(k) \exp(j2\pi F(t - T_g)k), \quad 0 \leq t < T_{sym} \quad (1)$$

where \mathbf{X}_{mi} is a serial data sequence.

All symbols except the frame guard interval and PSS are standard OFDM symbols, modulated with quadrature amplitude modulation (QAM). Only 4QAM and 16QAM have been observed thus far [Humphreys et al., 2023]. The SSS is anchored with a fixed initial phase relative to the PSS, whereas most following symbols exhibit a $\pi/4$ phase shift with respect to the PSS, as observed in [Humphreys et al., 2023]. One such symbol is the final OFDM symbol, which is 4QAM but has a $\pi/4$ phase offset relative to the PSS.

Table I provides a concise presentation of Starlink's downlink signal parameters. Fig. 2 provides a pictorial view of the frame and channel space.

B. Symbol generation

Starlink's downlink signal consists of 8 channels each F_s wide, with a channel guard of F_g between them, placed within the 10.7 – 12.7GHz frequency band. The i th channel is centered at F_{ci} , as expressed in Table I. Due to the large amount of data to be generated by a signal simulator, this paper will limit the simulator to a single channel, although a process for extending to multiple channels is trivial.

Algorithm 1 showcases the method used to generate a single symbol given a serial data sequence \mathbf{X}_{mi} . A discrete version of (1) is applied to the data sequence through the IFFT, followed by appending the cyclic prefix. Next, the signal is appropriately frequency shifted to account for a provided receiver center frequency F_{cr} relative to the channel center frequency F_c , followed by resampling to account for a provided receiver sampling frequency F_{sr} up to the channel bandwidth F_s . Finally, additive white

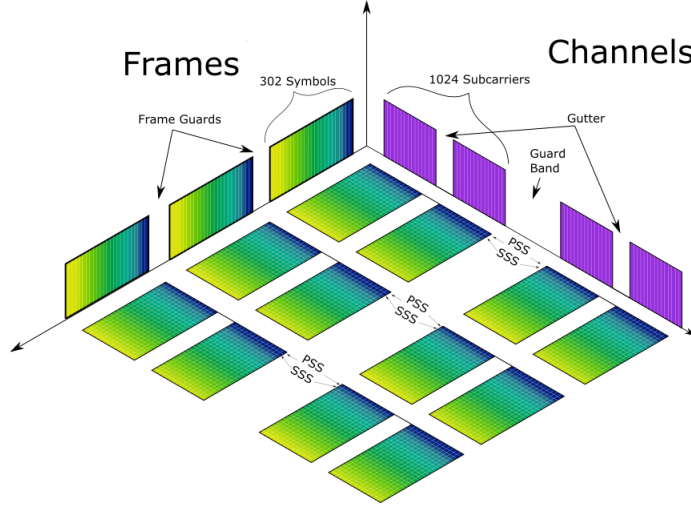


Fig. 2: Frame and Channel Layout of the Starlink Ku-band downlink signal depicting 3 consecutive frames and 2 channels.

Algorithm 1: $\text{genStarlinkOFDM}(\mathbf{X}_{mi}, \text{SNR}, F_c, F_{cr}, F_{sr})$

Input : $\mathbf{X}_{mi} \in \mathbb{C}^{N \times 1}$, SNR, F_c , F_{cr} , F_{sr}

Output: $\mathbf{x}_{mi} \in \mathbb{C}^{(N+N_g) \times 1}$

- 1 $\mathbf{x} = \text{IFFT}(\mathbf{X}_{mi})$
 - 2 $\mathbf{x}_{mi} = [\mathbf{x}(N - N_g - 2 : N - 1), \mathbf{x}(0 : N - 1)]$
 - 3 $\sigma_w = \sqrt{1/(2 \cdot \text{SNR})}$
 - 4 $\mathbf{t} = [0 : (N + N_g - 1)] / F_s$
 - 5 $\mathbf{x}_{mi} = \mathbf{x}_{mi} \odot \exp(j2\pi(F_c - F_{cr})\mathbf{t})$
 - 6 $\mathbf{x}_{mi} = \text{resample}(\mathbf{x}_{mi}, F_s, F_{sr})$
 - 7 $\mathbf{x}_{mi} = \text{AWGN}(\mathbf{x}_{mi}, \sigma_w)$
-

Gaussian noise (AWGN) is applied to the signal based on a provided signal-to-noise ratio (SNR). Fig. 3 shows spectrograms of concatenated symbols with different receiver center frequencies F_{cr} and receiver sampling rates F_{sr} .

C. Ephemeris Data and Doppler Model

Starlink currently offers ephemeris data for all their satellites. The data this paper utilizes are published in the Modified ITC file format including the SVs position, velocity, and covariances. Each file includes a 72-hour prediction, and the files are distributed every 8 hours at 4:30, 12:30, and 20:30 UTC [Sta, 2023]. The predictions provide estimates at 60-second steps. Alternatively, one could generate the appropriate position time histories to provide the simulator from data provided by NORAD.

Using the public ephemerides and a receiver location, one can trivially model the apparent Doppler of the signal. For illustrative purposes, a visual of the orbit of SV with ID 1800 on April 14th 2023 over a 15 minute interval starting at 17:04:42 is shown in Fig. 4, the information of which is used to generate a Doppler time history in Fig. 5. The signal's instantaneous Doppler f_d is calculated using (2), the equation for apparent Doppler given the relative velocity between the SV and the receiver, $\mathbf{v} \in \mathbb{R}^3$, the signal's wavelength λ , and the relative distance between the SV and the receiver, $\mathbf{r} \in \mathbb{R}^3$.

$$f_d = -\frac{1}{\lambda} \mathbf{r}^\top \cdot \mathbf{v} \quad (2)$$

When using estimates provided every 60 seconds, the interpolation between the points may not be accurate if too few points are provided. Offering less than 15 minutes of the ephemeris data for interpolation leads to a near-linear or constant Doppler time history model. To avoid making assumptions on the Doppler model, the choice will be left to the user. The simulator applies a user-provided Doppler time history by generating a phase time history $\Theta[n]$ re-sampled at the full channel bandwidth F_s . The phase time history is the discretized version of $\Theta(t) = \int_0^t f_d(\tau) d\tau$, using a cumulative sum. Alternatively, the simulator can intake a constant CFO to apply to the simulated signal for a constant Doppler model.

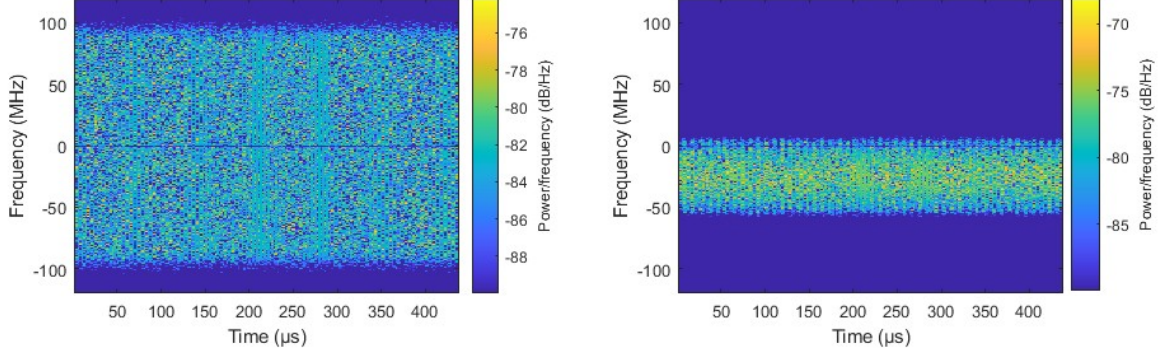


Fig. 3: Spectrograms of 100 concatenated symbols, with $F_{sr} = 200\text{MHz}$ and $F_{cr} = F_{c6}$ (left) and with $F_{sr} = 62.5\text{MHz}$ and $F_{cr} = F_{c6} - 25 \cdot 10^6$ (right), generated with an SNR of 15dB.



Fig. 4: Visualization of orbit over receiver location in Austin.

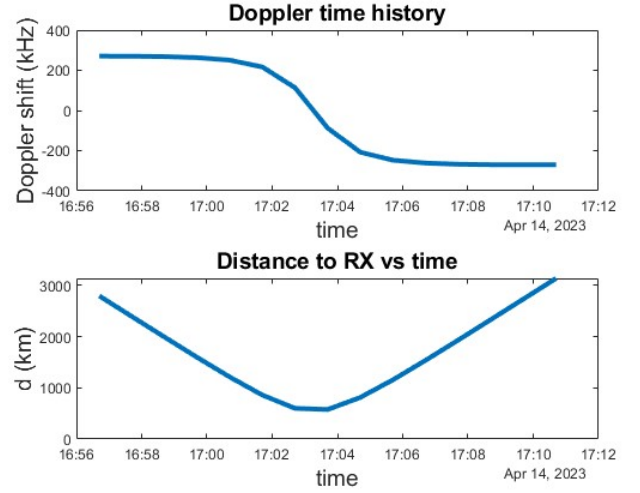


Fig. 5: Calculated Doppler to receiver in Austin.

D. Frame generation

Generating an entire frame amounts to concatenating symbols generated by Algorithm 1. If the algorithm is used on each symbol individually, it may result in artifacts from concatenating symbols in time that were resampled individually. To avoid such issues, it is best to resample to F_{sr} and apply the Doppler time history only after an entire frame is formed.

Suppose a desired SNR, Starlink channel center F_c , receiver center frequency F_{cr} , receiver sampling rate F_{sr} , desired Doppler time history, and phase are provided. Further, suppose we can generate the PSS in accordance with [Humphreys et al., 2023] and also generate the SSS using Algorithm 1 and the SSS sequence $\mathbf{X}_{m,1}$, both symbols with appropriate noise. After generating the remaining $N_{sf} - 2$ symbols with AWGN, we can generate the phase history from the Doppler history, concatenate the symbols in a single vector, append the frame guard and prepend some guard to emulate a delay. Further, we can apply the frequency shift F_{cr} to account for the receiver center frequency, apply the phase history to account for the Doppler, and finally resample at F_{sr} to account for the receiver sampling rate to form a frame. Algorithm 2 follows this process, as indicated by generating symbols with F_s , followed by resampling after the concatenation of the symbols.

The process can be further extended to concatenate frames into streams simulating longer data captures, randomly placing frames to emulate the frame pattern of the Starlink downlink signal transmission. For the simulator developed in this paper, a binomial random variable is used, even though frames are more likely to appear in bursts rather than as a binomial random variable. Notably, we resample to F_{sr} and applying the Doppler time history only after the stream is formed to avoid any artifacts.

Algorithm 2: genStarlinkFrame($\mathbf{X}_m, \text{SNR}, F_c, F_{cr}, F_{sr}, \tau_0, \mathbf{f}_{\text{hist}}$)

Input : $\mathbf{X}_m \in \mathcal{C}^{N \times N_{\text{sf}}}$
 $\text{SNR}, F_c, F_{cr}, F_{sr}, \tau_0$
 $\mathbf{f}_{\text{hist}} \in R^{(T_f F_s) \times 1}$
Output: $\mathbf{x} \in \mathcal{C}^{(T_f + \tau_0) F_{sr} \times 1}$

- 1 $\mathbf{x}_{m0} = \text{genPSS}(\text{SNR}, F_c, F_s, F_s)$
- 2 $\mathbf{x}_{m1} = \text{genStarlinkOFDM}(\mathbf{X}_{m1}, \text{SNR}, F_c, F_s, F_s)$
- 3 $\mathbf{x}_g = \text{AWGN}(\text{zeros}(F_s \cdot T_{\text{fg}}, 1), \sqrt{1/(2\text{SNR})})$
- 4 $\mathbf{x}_{\text{lag}} = \text{AWGN}(\text{zeros}(F_s \cdot \tau_0, 1), \sqrt{1/(2\text{SNR})})$
- 5 for $i = 2$ to $N_{\text{sf}} - 1$
- 6 $\mathbf{x}_{mi} \leftarrow \text{genStarlinkOFDM}(\mathbf{X}_{mi}, \text{SNR}, F_c, F_s, F_s)$
- 7 end
- 8 $\mathbf{x} = [\mathbf{x}_{\text{lag}}, \mathbf{x}_{m0}, \mathbf{x}_{m1}, \dots, \mathbf{x}_{mN_{\text{sf}}}, \mathbf{x}_g]$
- 9 $\phi_{\text{hist}} = \text{cumSum}(\mathbf{f}_{\text{hist}} - \mathbf{f}_{\text{hist}}(0))$
- 10 $\mathbf{t} = [0 : (T_f + \tau_0)F_s] / F_s$
- 11 $\mathbf{x} = \mathbf{x} \odot \exp(j2\pi(F_c - F_{cr})\mathbf{t}) \odot \exp(j\phi_{\text{hist}})$
- 12 $\mathbf{x} = \text{resample}(\mathbf{x}, F_s, F_{sr})$

IV. ACQUISITION AND DETECTION

Acquisition of the signal can follow two paths: data-aided and non-data-aided. The latter would depend on the cyclic nature of the OFDM symbols by correlating the incoming signal with one captured with a T delay, presenting a peak due to the cyclic prefix in each symbol. The former depends on knowledge of symbols within the signal to correlate against, namely the PSS and SSS. This paper will follow the data-aided approach.

Acquiring the signal, or obtaining estimates of the TOA and frequency of arrival (FOA), depend on generating a complex ambiguity function (CAF). The CAF is parametrized by the frame's time offset compared to the locally generated symbols, and the Doppler frequency.

After analyzing the statistical properties of the samples generated by the CAF, a standard Neyman-Pearson hypothesis test can be used to declare a detection. The coordinates of the detected peak on the CAF reveal the TOA and the effective carrier frequency offset (CFO) through the FOA.

A. Complex Ambiguity Function

Suppose the received signal \mathbf{y} is resampled from the receiver sampling rate F_{cr} to the full channel bandwidth F_s , and frequency shifted to be centered at the closest Starlink channel center F_c rather than the receiver center frequency F_{cr} . For some constant CFO β , the received signal is considered to be:

$$\mathbf{r} = \text{resample}(\mathbf{y}, F_{cr}, (1 - \beta)F_s) \odot \exp(-j2\pi[(\beta + 1)F_c - F_{cr}]\mathbf{t}), \quad \mathbf{t} = \left[0, 1, \dots, \dim(\mathbf{y}) \frac{F_s}{F_{sr}}\right] / F_s \quad (3)$$

(4)

The signal $r(n)$ may be cross correlated with a known sequence, denoted $c(n)$, also sampled at F_s and centered at F_c . If $c(n)$ involves non-consecutive symbols, these must be appropriately zero-padded to preserve their relative phase. Let N_c denote the number of non-zero samples in $c(n)$, and let N_a denote its overall length.

For arbitrary complex-valued sequences $a(n)$ and $b(n)$, define the correlation function $R_{ab}(k)$ as

$$R_{ab}(k) \triangleq \sum_{n=0}^{N_a-1} a(n+k)b^*(n) \quad (5)$$

The cross correlation between $r(n)$ and $c(n)$, written as $R_{rc}(k)$, can be used to estimate the relative time offset τ_0 between the two, since the value of k at which a peak appears in $R_{rc}(k)$ is the sample offset corresponding to τ_0 .

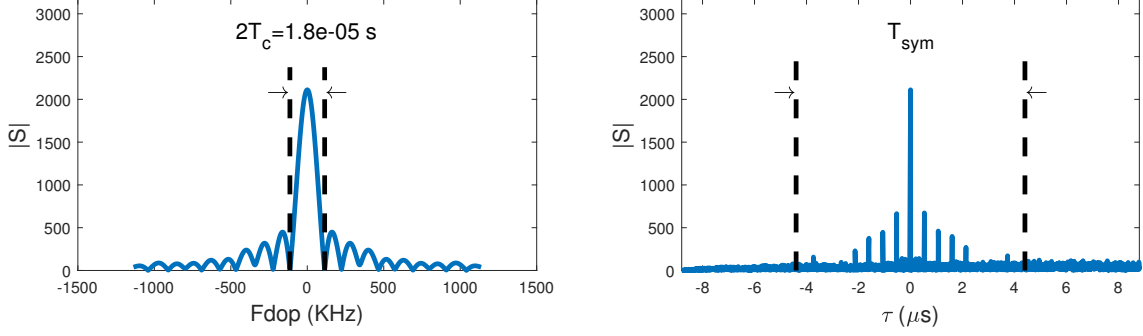


Fig. 6: CAF slices at $S(f, 0)$ (left) and $S(0, k)$ (right) using a generated frame with no noise and the PSS and SSS concatenated as the known sequence.

The statistical properties of the known sequence $c(n)$ are as follows:

$$\mathbb{E}[c(n)] = 0, \quad n \in [0, N_a - 1] \quad (6)$$

$$\mathbb{E}[R_{cc}(0)] = \sum_{n=0}^{N_c-1} \mathbb{E}[c(n)c^*(n)] = N_c \sigma_c^2 \quad (7)$$

$$\mathbb{E}[c(n)c^*(k)] = 0, \quad n \neq k \quad (8)$$

These properties hold because the complex serial data sequence X_{mik} is modeled as zero mean with independent and identically distributed (iid) elements each having variance σ_c^2 . To estimate the CFO, we expand the search domain to include β by calculating $R_{rc}(k)$ over different versions of $r(n)$ as given in (3) generated across a range of β values.

$$S(f, k) = \sum_{n=0}^{N_a-1} r(n+k) \cdot c^*(n) \cdot \exp(-i\hat{\theta}_f(n)) \quad (9)$$

where $\hat{\theta}_f$ is the estimated to Doppler-introduced phase, a function of f .

Suppose the received signal is modeled as follows:

$$r(n) = A(n)x(n) \exp(i\theta_{f_D}(n)) + w(n) \quad (10)$$

for some time-varying signal amplitude A , and actual carrier phase offset θ_{f_D} along with Gaussian noise w . Here, $x(n)$ is the Doppler-corrected, digitized, and resampled version of the signal without noise. Ideally, $c(n)$ makes up a subset of the samples in $x(n)$. Since the signal $r(n)$, and thus $x(n)$, will be multiplied with $c(n)$ and coherently summed, the resulting sweep over various phase offsets k will result in the autocorrelation of c . Using the fact that the amplitude, signal, and phase are uncorrelated, and using an assumption that over the accumulation period the amplitude remains near some average value \bar{A} , (9) is approximately:

$$S(f, k) \approx \bar{A}R_{xc}(k) \left[\frac{1}{N_a} \sum_{n=0}^{N_a-1} \exp(i\Delta\theta(n)) \right] + n_k \quad (11)$$

where $R_{xc}(k)$ is the cross correlation of x and c non-normalized as defined in (5), $\Delta\theta(n) = \theta_{f_D}(n) - \hat{\theta}_f(n)$, and $n_k = \sum w(n)c^*(n) \exp(-i\hat{\theta}_f(n))$. It can be shown that the average phasor value is $\text{sinc}(\Delta f T_c)$, for $\Delta f = f_D - f$ and T_c the period in seconds corresponding to N_c [Holmes, 2007].

Assuming a consecutive sequence is known, the standard analytical equation for a CAF in (12) applies, otherwise a more complicated shape with taller sidelobes is evident, though with the same peak value. Using the simulator to generate a frame, one can use (9) to generate the CAF. Fig. 6 shows the CAF slices at $S(0, k)$ and $S(f, 0)$ for a frame generated with no Doppler or delay.

$$S(f, k) \approx \bar{A}R_{xc}(k)\text{sinc}(\Delta f T_c) + n_k \quad (12)$$

B. Hypothesis Testing Scenarios

Suppose we perform the cross correlation as expressed so far. The results of the different $R_{rc}(k)$ values generated from the different CFOs and time offsets fall into scenarios: (1) only noise, (2) an unaligned signal with additive noise, (3) an aligned signal with additive noise. We can represent the detection problem as a 3-case hypothesis test:

$$r(n) = \begin{cases} w(n), & \text{under } H_0 \\ Ax(n+k) + w(n), & \text{under } H_1 \\ Ax(n) + w(n), & \text{under } H_2 \end{cases} \quad (13)$$

The noise is distributed as an iid complex Gaussian random process $w(n) \sim \mathcal{CN}(0, \sigma_w^2)$. The variance σ_w^2 is the sum of the real and imaginary variances: $\sigma_w^2 = \sigma_{\Re(w)}^2 + \sigma_{\Im(w)}^2$. In the case where the real and imaginary components are iid, then $\sigma_{\Re(w)}^2 = \sigma_{\Im(w)}^2 = \sigma_w^2/2$.

The statistic to be used in the hypothesis testing is $S_k \triangleq |R_{rc}(k)/\sigma_0|^2$, where $R_{rc}(k)$ is the value of the correlation function from (5) and σ_0 is defined in A-A. Under all hypotheses considered, this involves a sum of N_c samples of a random variable produced by multiplying $r(n)$ with $c^*(n)$. Due to the central limit theorem (CLT), the result of the sum can be modeled as a complex Gaussian random variable (GRV) with an arbitrary angle θ . It can be shown that for a univariate complex GRV $x \sim \mathcal{CN}(0, 1)$, the magnitude squared follows a Chi Squared distribution with 2 degrees of freedom $|x|^2 \sim \chi_2^2$. It is also known that for a complex $x = x_R + x_I i$ with $x_R \sim \mathcal{N}(\mu \cos(\theta), 1)$ and $x_I \sim \mathcal{N}(\mu \sin(\theta), 1)$, the magnitude squared follows a non-central Chi Squared distribution with two degrees of freedom and a non-central parameter of μ^2 , or $|x|^2 \sim \chi_2^2(\mu^2)$. Finally, for a complex GRV $x \sim \mathcal{CN}(0, \sigma^2)$, the magnitude squared follows a gamma distribution with shape parameter 1 and scale parameter σ^2 , or $|x|^2 \sim \Gamma(1, \sigma^2)$.

For the analysis of each scenario, refer to the Appendices A-A, A-B, and A-C, which assume the received signal is originally sampled at F_s . In the case where it is sampled at F_{sr} and artificially resampled as in (3), then a scaling of F_{sr}/F_s has to propagate through the results to account for a reduction in correlation power since the local replica is now only correlated against a received signal with power only within F_{sr} . The results may be summarized as follows:

$$S_k = |R_{r,c}(n)/\sigma_0|^2 \sim \begin{cases} \chi_2^2 & H_0 : \text{no frame} \\ \Gamma(1, 2\sigma_1^2/\sigma_0^2) & H_1 : \text{unaligned} \\ \chi_2^2(\lambda) & H_2 : \text{aligned} \end{cases} \quad \text{where} \quad \begin{cases} \sigma_0^2 = \frac{\sigma_w^2 \sigma_c^2 N_c}{2} \frac{F_{sr}}{F_s} \\ \sigma_1^2 = \frac{N_c \sigma_c^2 \sigma_w^2 (\text{SNR}+1)}{2} \frac{F_{sr}}{F_s} \\ \lambda = \left(\frac{N_c A \sigma_c^2 F_{sr}}{\sigma_0} \right)^2 \end{cases} \quad (14)$$

The three scenarios are clearly visible in Fig. 7, which is the cross-correlation of the Doppler-corrected signal with the local replica, a slice of the CAF along the frequency-maximizing value. The peak is H_2 , the lower noise floor is H_0 , and the raised noise floor is H_1 . A detection for purposes of TOA estimation falls under the third scenario, H_2 , while a detection of a frame falls under the second or third scenarios. The parameters describing the distributions for the statistic S_k are the noise variance σ_w^2 , signal power $P_s = A^2$, the non-zero known portion variance σ_c^2 and non-zero known portion length N_c .

Once a peak is identified corresponding to the local replica in the received signal, the post-correlation SNR of that peak can directly lead to an estimate of the pre-correlation SNR with the following relationship:

$$\text{SNR} = \frac{\text{SNR}_{\text{post}}}{\sigma_c^2 N_c F_{sr}/F_s} \quad (15)$$

One can choose a threshold to meet a false alarm probability for H_1 that will encompass samples from H_0 . This is clearly visible in Fig. 7, where the threshold based on H_0 is lower than that based on H_1 . The hypothesis test can be re-framed as a binary hypothesis test. If the threshold based on H_0 is chosen, the raised noise floor samples from H_1 would trigger a detection. In the case where the statistic to be compared to the threshold is the maximum over the CAF generated from an interval, this will almost always be the peak but may also be triggered by the raised noise floor under low SNR scenarios. If the threshold based on H_1 is chosen, the raised noise floor samples from H_1 no longer count as a detection. This second case can be more useful, since once it is determined, the threshold can be applied to the output of a matched filter of the Doppler-corrected received signal with the local replica. An important note here is, for low SNR, the two noise floors converge making the choice moot since the thresholds also converge.

C. Probability of Detection

The probability of detection P_D depends on the false alarm probability we are willing to accept. To be explicit about the false alarm probability, consider the probability of false alarm $P_{f_{\text{cell}}}$ of a single cell in the CAF, and the probability of false alarm over the entire CAF P_f , where

$$P_f = 1 - (1 - P_{f_{\text{cell}}})^{N_{\text{grid}}}$$

over a grid of size N_{grid} of TOA and FOA pairs [Borio et al., 2008]. The threshold value is then found from the inverse cumulative distribution function of the Chi Squared distribution for H_0 or the Gamma distribution for H_1 from (14) using $P_{f_{\text{cell}}}$. The choice of distributions is based on the discussion in Sec. IV-B on the two thresholds. Values above the threshold s^* are deemed detections; values below the threshold are not.

$$s^* = F_i^{-1}(P_{f_{\text{cell}}}) \quad (16)$$

In (16) above, F_i^{-1} is the inverse cumulative distribution function determined by the hypothesis H_i . Fig. 7 showcases the two thresholds that can be chosen, where the lower threshold was generated based on the Chi Squared distribution for H_0 and the higher threshold was generated based on the Gamma distribution for H_1 .

The probability of detection will vary based on our choice of threshold, and thus definition of a true detection. Choosing the H_0 threshold s_0^* implies we accept all H_1 samples as true detections along with the H_2 samples. Choosing the H_1 threshold s_1^* implies we only accept the H_2 samples as true detections. The H_1 samples previously accepted as detections are now false alarms.

Another factor in determining the probability of detection is how we choose the statistic to be compared against the threshold. A typical way, and one also discussed in [Borio et al., 2008], is to choose a maximum over a set of samples. In the H_1 threshold case, this implies the probability of detection is simply based on the inverse CDF of the non-central Chi Squared distribution. In the H_0 threshold case, the process is slightly more complicated, as now a true detection will occur if any of the H_1 samples or the single H_2 sample from the CAF exceed the threshold. Using the complement rule, and approximating the CAF samples as iid, we can form the probability of detection as follows:

$$P_D = \begin{cases} 1 - (1 - F_2(s^*))(1 - F_1(s^*))^{N_{H_1}} & , s^* = s_0^* \\ 1 - F_2(s^*) & , s^* = s_1^* \end{cases} \quad (17)$$

where $F_2(s^*) = Q_1(\sqrt{\lambda}, \sqrt{s^*})$ is the Marcum Q-function of order 1, $F_1(s^*)$ is the CDF of the Gamma distribution, and N_{H_1} is the number of H_1 samples in the CAF.

With the process as described, an extension for non-coherent summations of statistics becomes trivial. For N_{nCS} non-coherent summations, the simplified 2-case hypothesis test for each of the two definitions of a detection now follow that of (18).

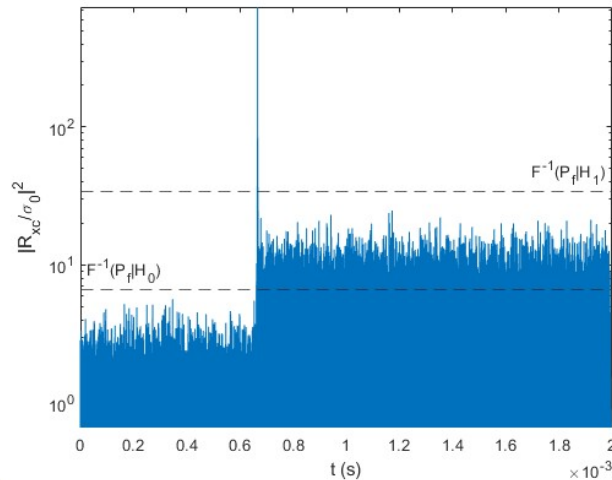


Fig. 7: Figure of the two thresholds that can be chosen, using a generated frame against a known sequence of the PSS and SSS concatenated at 5 dB SNR and $F_{\text{sr}} = 62.5$ MHz.

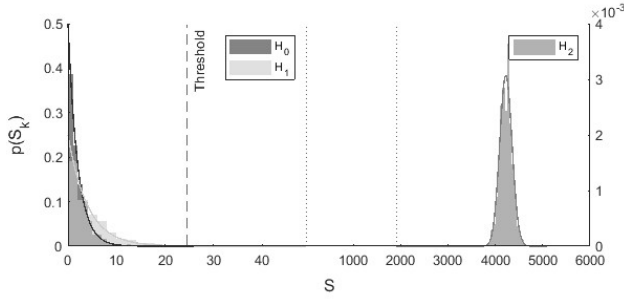


Fig. 8: Histogram of statistic generated from 500 frames for each scenario, at 0 dB SNR with coherent integration over a single frame, overlaid by their theoretical distributions.

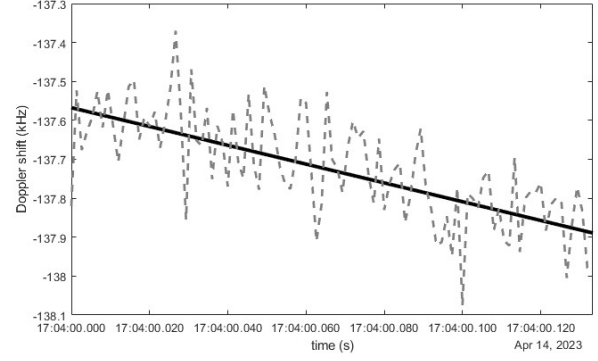


Fig. 9: Acquisition and tracking of Doppler of 100 consecutive simulated Starlink frames using true ephemerides.

$$Z = \sum_{k=1}^{N_{ncs}} S_k \sim \begin{cases} \chi_{2 \cdot N_{ncs}}^2 & H_0' : \text{no detection} \\ \chi_{2 \cdot N_{ncs}}^2(\lambda \cdot N_{ncs}) & H_1' : \text{detection} \end{cases} \quad \text{or} \quad \begin{cases} \Gamma(N_{ncs}, 2\sigma_1^2/\sigma_0^2) & H_0' : \text{no detection} \\ \chi_{2 \cdot N_{ncs}}^2(\lambda \cdot N_{ncs}) & H_1' : \text{detection} \end{cases} \quad (18)$$

The threshold and probability of detection are also trivially extendable since, for example, the CDF of the non-central Chi-Squared simply adapts the Marcum Q-function order to N_{ncs} . Similarly, the Gamma distribution's shape parameter becomes N_{ncs} .

V. RESULTS

To showcase the utility of the simulator and the accompanying tools, this section will show : (1) the hypothesis testing scenario distributions from generated CAFs, (2) a Doppler-time history generated from a simulated capture, (3) a P_D vs SNR plots under various scenarios, and (4) detection of a captured signals.

A. Simulated Results

To verify the simulator follows the ideas presented in this paper, a variety of scenarios are generated. First, to confirm the distributions of samples from the CAF described in Sec. IV-B, a number of values representing the statistic S_k from (14) are generated. These statistic values are generated using simulated frames under H_0 , H_1 , and H_2 with the local replica consisting of just the PSS and SSS as in (9). The normalized histogram of the statistic under each scenario is found to match the theoretical distributions from (14) in Fig. 8, and holds for any SNR and F_{sr} values.

Next, to showcase the applied Doppler-time history, we generate a capture using a Doppler-time history derived from estimates of Starlink's satellite positions. The ephemeris data are from the segment mentioned in Section III-C. The generated capture consists of 100 consecutive generated frames. To confirm the frames follow the provided Doppler-time history, the capture is segmented in blocks lasting T_{sym} . A CAF is generated for each block to estimate the Doppler frequency. Fig. 9 shows the Doppler frequency estimates sampled at each block overlaying the input Doppler time history.

B. Signal Detection Sensitivity

Based on the results in Sec. IV, we can explore the probability of detection of a frame for various SNRs. To confirm the theoretical P_D vs SNR equation in (17), we can run a Monte-Carlo simulation by generating 500 frames, each time sweeping over different SNRs and tallying up the detections. For this simulation, we are using the conservative threshold s_1^* discussed in Sec. IV-C, with $P_{f_{cell}} = 10^{-8}$. Fig. 10 shows the curves for various coherent integration periods, dictated by the number of known symbols in the local replica. Notably, doubling the integration period results in a 3 dB decrease in the minimum SNR required to detect the frame, for the same P_D . A welcome result is that for a $P_D = 0.95$, and just the PSS, we can detect frames as low as -15.7 dB for received signals sampled at F_s .

Next, we can check how non-coherently summing statistics will affect the P_D . This time, summing up 2 consecutive statistics from the simulation, results in the curves in Fig. 11, also matching the theoretical curve. A notable result here is the decrease

in minimum SNR by 2.6 dB compared to the single integration period with the same local replica. These curves also assume a received signal sampled to view an entire channel.

One variation to the simulation is a signal sampled at F_{sr} . This results in an increase in the minimum SNR due to a decrease in the correlation power of the narrower band signal against the full band local replica. The shift in the curve is roughly equal to the ratio F_{sr}/F_s , resulting in an increase of approximately $-10 \log(F_{sr}/F_s)$ dB depending on how well the signal is filtered, or on the user's knowledge on the filter's shape.

Another variation is running the simulation with the more lenient threshold s_0^* . For a generated signal sampled at F_s , the s_0^* threshold only results in about a 0.1 dB decrease in the minimum SNR. Fig. 12 showcases the scenario of a signal sampled at F_{sr} with both thresholds, showing roughly a 0.2 dB decrease in the minimum SNR. Fig. 12 also shows the increase of $-10 \log(F_{sr}/F_s)$ dB when compared to the F_s curve for 2 known symbols in Fig. 10.

The misalignment with the theoretical curves in Fig. 12 is due to non-ideal filtering causing the simulated H_2 sample values presenting as lower than expected. The even-further misalignment from the theoretical curve for the s_0^* curve is further attributed to the faulty assumption of iid H_1 samples. The process resamples the received signal back to F_s , introducing correlation between samples. If any of the samples tend to be higher, then the surrounding H_1 samples also tend to be higher, leading to a higher P_D . Additionally, calculating the P_D under this case requires the expected number of H_2 samples from (17). The analytical solution for P_D can then at least be thought of as a lower bound, as added information could refine the bound.

C. Empirical Results

We collected data using hardware and software described in [Qin et al., 2023] to evaluate the tools from this paper, as well as note some differences. One indication of the simulator's frame working properly is by comparing the autocorrelation of an empirical and simulated frame. Fig. 13 shows that the autocorrelation matches the empirical one. A similar comparison is made in [Humphreys et al., 2023], where the empirical autocorrelation suffered from additional correlation caused by aliasing noise in the captures, shown in Fig. 3 of that paper. Once the aliasing is removed, the autocorrelation yields the tighter patterns shown in Fig. 13 of this paper.

Recently, in [Blázquez-García et al., 2023] and [Qin et al., 2023], the notion of a fixed interval over which satellites are guaranteed to have a fixed beam is introduced. This fixed assignment interval (FAI) seems to last around 15 seconds. The simulator does not incorporate this observation in its capture generation. Additionally, the implication that side-beams from a SV intended for neighboring cells could be exploited for TOA measurements is not something the simulator can generate automatically. These side-beams arrive at different power levels and timing compared to the assigned-beam. This is not a limitation of the simulator, however, since it could be used over multiple runs to generate signals of varying power and timing which the user can add together to emulate the empirical captures.

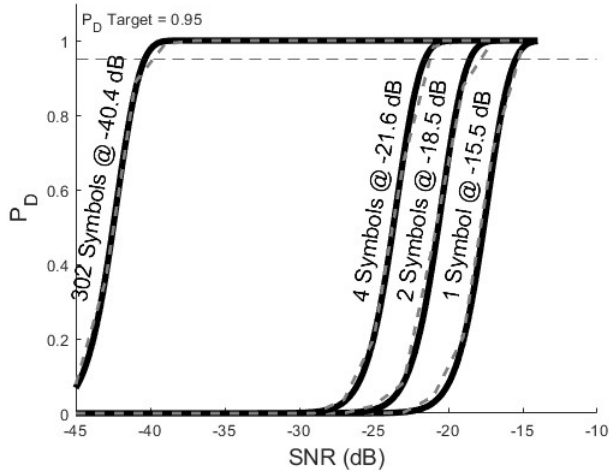


Fig. 10: Analytical (solid) and simulated (dashed) PD vs SNR curves with coherent integration over a single frame for various quantities of known symbols.

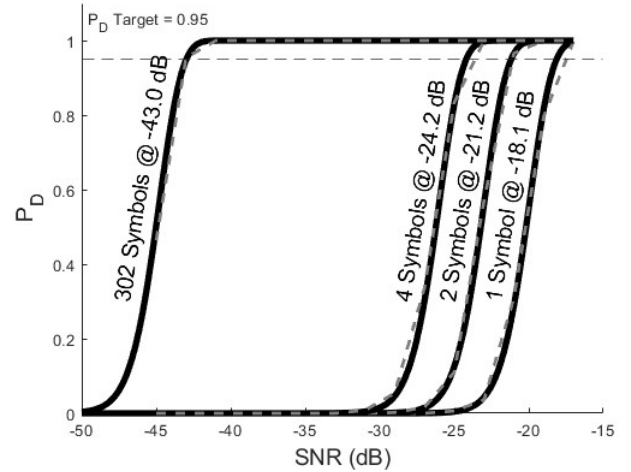


Fig. 11: Analytical (solid) and simulated (dashed) PD vs SNR curves with N_{ncs} non-coherently summed coherent integrations over a single frame for various quantities of known symbols.

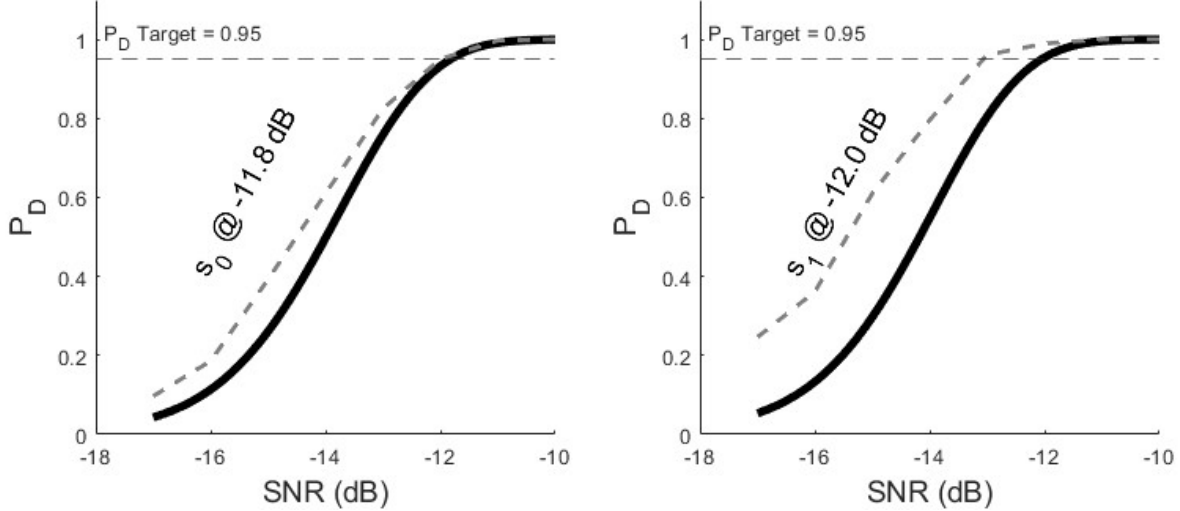


Fig. 12: Analytical (solid) and simulated (dashed) PD vs SNR curve with coherent integration over a single frame for the PSS and SSS with $F_{sr} = 62.5$ MHz filtered to 53.12 MHz using s_1^* (left) and s_0^* (right). The theoretical minimum SNR to detect a frame at $P_D = 0.95$ for each is displayed on the figure.

The presence of the side-beams cause implication in the simulator and analysis in the form of assumptions about the lower floor. As mentioned in previous sections, the lower noise floor can help determine the pre-correlation SNR, and can also be used to estimate the noise variance – a necessary estimate for the threshold. Imagine a scenario like that depicted in Fig 7, in which there is a clear lower noise floor before a frame. If that floor includes a lower-power side-beams the pre-correlation SNR estimate, and thus the probability of detection, would be affected.

Fig. 14 is the real world example of the simulated version of Fig 7. Using the first T_f of the interval shown, we can find an estimate of the Doppler to apply to the rest of the data. Correlating the Doppler-corrected data with the PSS and SSS results in easily distinguishable frames, especially with our H_1 threshold. An example of the difference with the simulated signal lies perfectly at 0.01 s into the interval, where a lower-power peak is present. This does not meet the higher threshold, even though it is most likely a frame observed from a side-beam. This presents the issue of having to recalculate the H_1 threshold for each interval, since the SNR estimate may drastically change due to the assigned-beam or side-beam ambiguity. Fig. 15 provides an empirical example of stronger side-beams that end up meeting the H_1 threshold.

The issue of timing is also possibly present in Fig. 14, as the peak between 0.004 s and 0.006 s is another possible side-beam with a timing offset away from a multiple of the assigned beam. Based on the peak of the presumed assigned beam frames and the noise floor, the SNR in Fig. 14 is around 0.4 dB, while for the side-beam at 0.01 seconds is around -14.5 dB. In Fig 15 the assigned beams are around 0.7 dB SNR, while the side-beams are around -4.81 dB. For our receiver sampling rate around 62.5 MHz, and a $P_{f,cell} = 10^{-8}$, the probability of detection with 2 symbols at -14.5 dB is 0.48, which seems reasonable for the side-beams from Fig. 14 teetering around the H_0 threshold.

VI. CONCLUSION

With the work from this paper, a Starlink Ku-band downlink signal that meets all currently known criteria in terms of signal structure and channel effects can easily be generated. Further, the acquisition analysis and procedure applied to simulated and empirical signals in this paper enable further study of Starlink's downlink signal. Using the ephemeris intake capability of the University of Texas Starlink Signal Simulator, one can study obtaining pseudoranges through simulation. Finally, this paper demonstrated detection of a real Starlink signal as low as -14.5 dB. For convenience, a MATLAB based implementation of the simulator is available at <https://gitlab.com/radionavlab/public>.

ACKNOWLEDGMENTS

Research was sponsored by the U.S. Department of Transportation (USDOT) under the University Transportation Center (UTC) Program (CARMEN+), and by affiliates of the 6G@UT center within the Wireless Networking and Communications Group at The University of Texas at Austin.

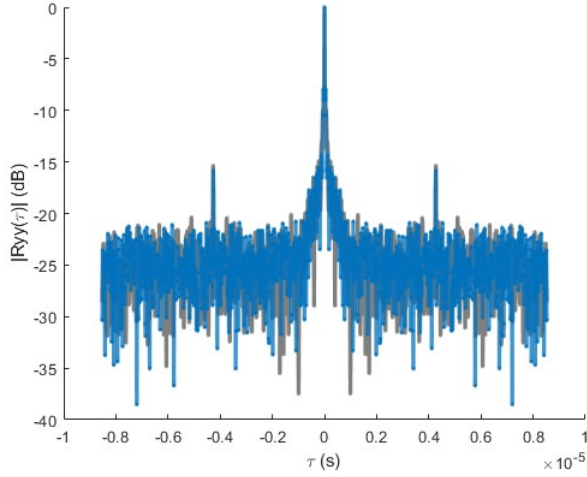


Fig. 13: Normalized cyclic autocorrelation function at $\alpha = 0$ for an empirical Starlink signal (blue), and for a simulated frame with iid Gaussian 4QAM symbols (gray).

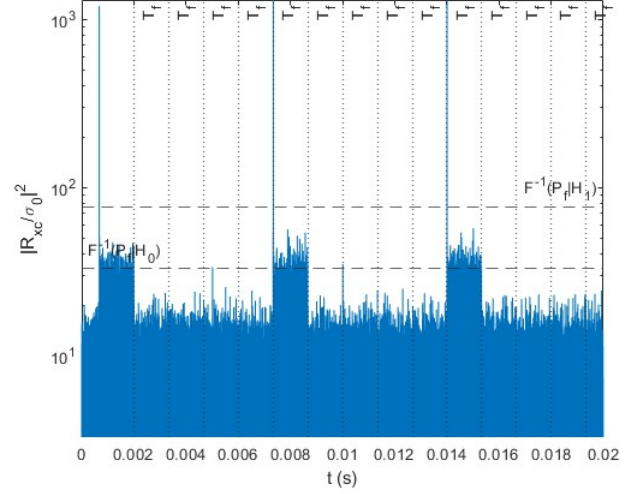


Fig. 14: Correlation of empirical Starlink data against a local PSS and SSS replica after Doppler compensation.

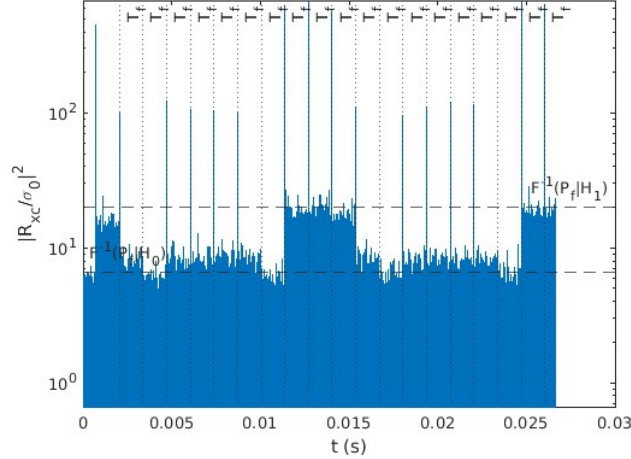


Fig. 15: Correlation of empirical Starlink data against a local PSS and SSS replica after Doppler compensation.

APPENDIX A HYPOTHESIS TESTING SCENARIO STATISTICAL ANALYSIS

A. Null Hypothesis

As expressed in (13), the null hypothesis H_0 assumes that $r(n) = w(n)$ for $n \in [0, N_a - 1]$. The mean and variance of the random variable resulting from multiplying $r(n)$ with $c^*(n)$ provide the parameters to describe the complex GRV resulting from the sum of N_c such random variables. For $n \in [0, N_a - 1]$, these are

$$\mu_{rc} = \mathbb{E}[r(n)c^*(n)] = 0 \quad (19)$$

$$\begin{aligned} \sigma_{rc}^2 &= \mathbb{E}[(w(n)c^*(n))(w(n)c^*(n))^*] - |\mathbb{E}[w(n)c^*(n)]|^2 \\ &= \mathbb{E}[w(n)w^*(n)] \mathbb{E}[c(n)c^*(n)] = \sigma_w^2 \sigma_c^2 \end{aligned} \quad (20)$$

Thus, for all k under H_0 , $R_{rc}(k) \sim \mathcal{N}(0, N_c \sigma_{rc}^2)$. If we define $\sigma_0^2 \triangleq \frac{\sigma_w^2 \sigma_c^2 N_c}{2}$, then the statistic $S_k = |R_{rc}(k)/\sigma_0|^2$ follows a Chi Squared distribution, or $S_k \sim \mathcal{X}_2^2$.

B. Hypothesis H_1

Under H_1 we assume $r(n) = Ax(n+k) + w(n)$. The process of determining the detection statistic distribution is equivalent to that for H_0 except for the variance of the random variable resulting from the multiplication of $r(n)$ and $c^*(n)$. In practice, for a very low SNR, the additional variance introduced by the signal's presence is negligible.

$$\mu_{rc} = \mathbb{E}[r(n)c^*(n)] = 0 \quad (21)$$

$$\begin{aligned} \sigma_{rc}^2 &= \mathbb{E}[(r(n)c^*(n))(r(n)c^*(n))^*] \\ &= A^2 \mathbb{E}[x(n)x^*(n)] \mathbb{E}[c(n)c^*(n)] \\ &\quad + \mathbb{E}[w(n)w^*(n)] \mathbb{E}[c(n)c^*(n)] \\ &= P_s \sigma_c^2 + \sigma_w^2 \sigma_c^2 = \sigma_c^2 \sigma_w^2 \left(\frac{P_s}{\sigma_w^2} + 1 \right) \end{aligned} \quad (22)$$

In (22), P_s denotes the power of the received signal without the noise. Identically to the H_0 case, $R_{rc}(k) \sim \mathcal{N}(0, N_c \sigma_{rc}^2)$ due to the CLT, but with a different expression for σ_{rc}^2 . The statistic $S_k = |R_{rc}(k)/\sigma_0|^2$ is now gamma distributed, due to the variance not being 1:

$$S_k \sim \Gamma(1, 2\sigma_1^2/\sigma_0^2) \quad \text{where} \quad \sigma_1^2 = \frac{(P_s \sigma_c^2 + \sigma_w^2 \sigma_c^2) N_c}{2} \quad \text{and} \quad \sigma_0^2 = \frac{\sigma_w^2 \sigma_c^2 N_c}{2} \quad (23)$$

C. Hypothesis H_2

Under H_2 we assume $r(n) = Ax(n) + w(n)$. The novelty of this hypothesis is that $x(n)$ contains some scaled version of our locally-generated signal c . The resulting sum of samples between $x(n)$ and $c^*(n)$ will be no different from the sum of the multiplication of $c(n)$ with $c^*(n)$ due to the zeroed-out portions of our local $c(n)$. A simplification can thus be made to view $r(n) = Ac(n) + w(n)$.

Since the resulting cross correlation will include the sum of $c(n)c^*(n)$, the mean value of the cross correlation will be biased away from zero on the real dimension. This is shown in (24) below.

$$\begin{aligned} \mu_R &= \mathbb{E}[R_{rc}(k)] = \mathbb{E} \left[\sum_{n=k}^{N_a-k-1} r(n)c^*(n) \right] \\ &= \sum_{n=k}^{N_a-1} \mathbb{E}[Ac(k)c^*(k)] = N_c A \sigma_c^2 \end{aligned} \quad (24)$$

To express the variance, it is useful to first express the second moment of the cross correlation:

$$\begin{aligned} \mathbb{E}[R_{rc}(k)R_{rc}^*(k)] &= \mathbb{E} \left[\left(N_c A \sigma_c^2 + \sum_{n=k}^{N_a-k-1} w(n)c^*(n) \right) \right. \\ &\quad \times \left. \left(N_c A \sigma_c^2 + \sum_{j=k}^{N_a-j-1} w(j)c^*(j) \right)^* \right] \end{aligned} \quad (25)$$

The sum of the product of the noise and local replica samples present in the second portion above is no different from H_0 except that there is a bias term $N_c A \sigma_c^2$ in the real dimension. This means that both unevaluated sums above form a GRV with zero mean and variance σ_0^2 , identical to the result from Appendix A-A with a mean of $N_c A \sigma_c^2$. To show the variance is in

fact the same as for H_0 , it is beneficial to observe the real and imaginary variances separately, the sum of which result in the complex random variable's variance:

$$\begin{aligned}\sigma_{\Im(R)}^2 &= \mathbb{E} [\Im(R_{rc}(k))^2] \\ &= \mathbb{E} \left[\left(\Im \left(\sum_{n=k}^{N_a-k-1} w(n)c^*(n) \right) \right)^2 \right] = \frac{\sigma_w^2 \sigma_c^2 N_c}{2}\end{aligned}\quad (26)$$

$$\begin{aligned}\sigma_{\Re(R)}^2 &= \mathbb{E} [\Re(R_{rc}(k))^2] - [\Re(\mu_R)]^2 \\ &= \mathbb{E} \left[\left(\Re \left(N_c A \sigma_c^2 + \sum_{n=k}^{N_a-1} w(n)c^*(n) \right) \right)^2 \right] \\ &\quad - (N_c A \sigma_c^2)^2 \\ &= \frac{\sigma_w^2 \sigma_c^2 N_c}{2} + (N_c A \sigma_c^2)^2 - (N_c A \sigma_c^2)^2 = \frac{\sigma_w^2 \sigma_c^2 N_c}{2}\end{aligned}\quad (27)$$

The result is that $R_{rc}(k) \sim \mathcal{N}(\mu_R, \sigma_{\Re(R)}^2 + \sigma_{\Im(R)}^2)$. The result of taking $S_k = |R_{rc}(\tau)/\sigma_0|^2$ is a non-central Chi Squared distribution, or $S_k \sim \mathcal{X}_2^2(\lambda)$, instead of the Chi Squared distribution from H_0 due to the non-zero mean.

$$\begin{aligned}S_k &\sim \mathcal{X}_2^2(\lambda) \\ \text{where } \lambda &= \left(\frac{N_c A \sigma_c^2}{\sigma_0} \right)^2 \text{ and } \sigma_0^2 = \frac{\sigma_w^2 \sigma_c^2 N_c}{2}\end{aligned}\quad (28)$$

REFERENCES

- [Sta, 2023] (2023). Starlink operators page. <https://www.starlink.com/satellite-operators>. Accessed: 2023-04-14.
- [Blázquez-García et al., 2023] Blázquez-García, R., Cristallini, D., Ummenhofer, M., Seidel, V., Heckenbach, J., and O'Hagan, D. (2023). Capabilities and challenges of passive radar systems based on broadband low-earth orbit communication satellites. *IET Radar, Sonar & Navigation*, n/a(n/a).
- [Borio et al., 2008] Borio, D., Camoriano, L., and Lo Presti, L. (2008). Impact of GPS acquisition strategy on decision probabilities. *IEEE Transactions on Aerospace and Electronic Systems*, 44(3):996–1011.
- [Du et al., 2021] Du, X., Song, T., Li, Y., Wu, M.-W., and Kam, P.-Y. (2021). An optimum signal detection approach to the joint ml estimation of timing offset, carrier frequency and phase offset for coherent optical ofdm. *Journal of Lightwave Technology*, 39(6):1629–1644.
- [Holmes, 2007] Holmes, J. K. (2007). *Spread Spectrum Systems for GNSS and Wireless Communications*. Artech House, 1st ed. edition.
- [Humphreys et al., 2023] Humphreys, T. E., Iannucci, P. A., Komodromos, Z. M., and Graff, A. M. (2023). Signal structure of the Starlink Ku-band downlink. *IEEE Transactions on Aerospace and Electronic Systems*, pages 1–16.
- [Iannucci and Humphreys, 2020] Iannucci, P. A. and Humphreys, T. E. (2020). Economical fused LEO GNSS. In *Proceedings of the IEEE/ION PLANS Meeting*.
- [Iannucci and Humphreys, 2022] Iannucci, P. A. and Humphreys, T. E. (2022). Fused low-earth-orbit GNSS. *IEEE Transactions on Aerospace and Electronic Systems*, pages 1–1.
- [Jardak and Adam, 2023] Jardak, N. and Adam, R. (2023). Practical use of Starlink downlink tones for positioning. *Sensors*, 23(6):3234.
- [Khalife et al., 2022] Khalife, J., Neinavaie, M., and Kassas, Z. M. (2022). The first carrier phase tracking and positioning results with Starlink LEO satellite signals. *IEEE Transactions on Aerospace and Electronic Systems*, 58(2):1487–1491.
- [Neinavaie and Kassas, 2022] Neinavaie, M. and Kassas, Z. M. (2022). Unveiling beamforming strategies of Starlink LEO satellites. In *Proceedings of the ION International Technical Meeting*.
- [Neinavaie et al., 2021] Neinavaie, M., Khalife, J., and Kassas, Z. M. (2021). Exploiting Starlink signals for navigation: First results. In *Proceedings of the ION GNSS+ Meeting*, pages 2766–2773, St. Louis, Missouri.
- [Neinavaie et al., 2022] Neinavaie, M., Khalife, J., and Kassas, Z. M. (2022). Acquisition, doppler tracking, and positioning with Starlink LEO satellites: First results. *IEEE Transactions on Aerospace and Electronic Systems*, 58(3):2606–2610.
- [Okati and Riihonen, 2022] Okati, N. and Riihonen, T. (2022). Nonhomogeneous stochastic geometry analysis of massive LEO communication constellations. *IEEE transactions on communications*, 70(3):1848–1860.
- [Psiaki, 2021] Psiaki, M. L. (2021). Navigation using carrier Doppler shift from a LEO constellation: TRANSIT on steroids. *Navigation, Journal of the Institute of Navigation*, 68(3):621–641.
- [Qin et al., 2023] Qin, W., Komodromos, Z. M., and Humphreys, T. E. (2023). An agile, portable antenna system for LEO megaconstellation-based PNT. In *Proceedings of the ION GNSS+ Meeting*.
- [Reid et al., 2020] Reid, T. G. R., Walter, T., Enge, P. K., Lawrence, D., Cobb, S., Gutt, G., O'Connor, M., and Whelan, D. (2020). *Position, Navigation, and Timing Technologies in the 21st Century: Integrated Satellite Navigation, Sensor Systems, and Civil Applications*, volume 1, chapter Navigation from Low Earth Orbit: Part 1: Concept, Capability, and Future Promise., pages 1359–1380. Wiley-IEEE.
- [SpaceX, 2021] SpaceX (2021). Revised SpaceX Gen2 non-geostationary satellite system, Technical Attachment. https://licensing.fcc.gov/myibfs/download.do?attachment_key=12943362. SAT-AMD-20210818-00105.
- [Xu, 2014] Xu, W. (2014). Sensing of OFDM signals in cognitive radio systems with time domain cross-correlation. *ETRI Journal*, 36(4):545–553.